Integrated Cathode-Electrolyte ($Li_{6.55}La_3Zr_{1.55}Ta_{0.45}O_{12}$/PEO-LiTFSI) Architecture Driven Excellent Performance of Solid-State Lithium Metal Batteries

Asish Kumar Das[a], Manish Badole[a], Hari Narayanan Vasavan[a], Samriddhi Saxena[a], Pratiksha Gami[a],
Neha Dagar[a], Sunil Kumar [a,b,*]

[a]Department of Metallurgical Engineering and Materials Science, Indian Institute of Technology Indore, Simrol, 453552, India

[b]Center for Electric Vehicle and Intelligent Transport Systems, Indian Institute of Technology Indore, Simrol, 453552, India

*Corresponding author E-mail: sunil@iiti.ac.in

Abstract:

The solid electrolytes in solid-state lithium batteries suffer due to low room temperature conductivity ($< 10^{-4}$ S cm^{-1}) and sluggish lithium-ion transport at the electrode-electrolyte interface. To fabricate solid-state lithium metal batteries employing composite solid electrolyte, Ta-doped $Li_7La_3Zr_2O_{12}$ (LLZTO) with room temperature conductivity ~ 6.1×10^{-4} S cm^{-1} was synthesized and dispersed in polyethylene oxide-lithium bis(trifluoromethanesulfonyl)imide (PEO-LiTFSI) polymer-salt matrix in different proportions. The sample SCE20 (20 wt.% LLZTO & 80 wt.% PEO-LITFSI), showing the best effective lithium-ion conductivity amongst all compositions (~ 1.44×10^{-4} S cm^{-1}), was used to fabricate lithium symmetric cells and all-solid-state cells with $LiFePO_4$ cathode in conjunction with lithium metal as the anode. The fabricated lithium symmetric cells showed high cyclability (more than 1100 hours) with a low overpotential of ~ 180 mV at a current density of ~ 0.4 mA cm^{-2}. The $LiFePO_4$ cells with monolithic cathode-SCE20 electrolyte architecture in conjunction with lithium metal as the anode exhibited ~ 50% lower interfacial resistance and delivered ~ 84.2% capacity retention after 1000 cycles at 1C with an initial discharge capacity of ~ 133 mAh g^{-1}. This facile, cost-efficient design of integrated cathode-electrolyte architecture by a doctor blade coating method can drive the application of solid-state lithium metal batteries on a commercial scale.

Keywords: All-solid-state cells; garnet; composite electrolytes; cathode-electrolyte interface; doctor-blade coating.

1. Introduction

The surging global demand for energy, coupled with the shift from traditional internal combustion engine vehicles to their electric counterparts, has prompted worldwide policymakers to seek highly efficient energy storage technologies. This pursuit aims to address the intermittent nature of renewable energy sources [1, 2]. Despite the dominance of lithium-ion technology in the rechargeable battery market for portable electronics over the last few decades, continuous innovation is imperative to outpace the evolving energy needs [3-5]. This innovation is driven by the necessity to meet specific energy requirements while addressing safety concerns associated with the use of organic flammable liquid electrolytes in state-of-the-art lithium-ion batteries [6].

All-solid-state lithium batteries (ASSLBs) with non-flammable solid electrolytes are emerging as the future energy storage technology [7]. This aims to mitigate the safety issues present in conventional Li-ion batteries. Moreover, incorporating lithium metal and high-voltage positive electrode materials could enhance the specific energy of ASSLBs. This enhancement is facilitated by the lithium dendrite suppression capability of solid electrolytes and the provision of a wide electrochemical stability window [8, 9]. However, the commercialization of ASSLBs faces challenges due to the high electrode-electrolyte solid-solid interfacial resistance of ceramic electrolytes and the low room-temperature ionic conductivity of solid polymer electrolytes [10-14]. While flexible solid polymer electrolytes could alleviate electrode-electrolyte resistance, their application in room-temperature ASSLBs is limited by low lithium-ion conductivity [15, 16]. Inorganic solid electrolytes like thio-LISICONs and Li-Argyrodites exhibit high Li-ion conductivity, surpassing even liquid electrolytes in terms of effective lithium-ion conduction [17-19]. Nevertheless, issues in the mass production of thin ceramic membranes and poor electrode-electrolyte interfaces hinder the widespread use of inorganic solid electrolytes. Various strategies, including surface treatments and adding buffer layers between the electrode and electrolyte, have been employed to address electrode-electrolyte interface issues [20-26].

The utilization of ceramic-polymer composite electrolytes capitalizes on the benefits of both components [14]. These composite electrolytes offer scalable processability, high ionic conductivity, good mechanical strength, and thermal stability at elevated temperatures [27]. Solid composite electrolytes (SCEs) are classified into ceramic-in-polymer solid electrolytes, comprising a higher weight percentage of ceramics, and polymer-in-ceramic solid electrolytes, featuring polymers infused in dominating ceramic matrices. In ceramic-in-polymer solid electrolytes, passive ceramics fillers act as plasticizers, facilitating polymer chain movement for facile lithium-ion conduction by reducing crystallinity in the polymer matrix [28-30]. Concurrently, lithium-ion conductive active ceramic fillers provide additional lithium-ion conduction paths through ceramic grains [31]. Additionally, ceramic fillers contribute to mechanical strength, resisting lithium dendrite growth. The suboptimal performance of various ASSLBs at room temperature is attributed to issues at the cathode-electrolyte interface and low lithium-ion diffusion kinetics on the cathode side. These challenges lead to significant specific capacity degradation at higher current densities [32]. Thus, the development of ASSLBs using solid composite electrolytes (SCEs) necessitates a low-cost cathode-electrolyte interfacial design, emphasizing the bulk lithium-ion conductivity of ceramic fillers [33]. The successful strategy of substituting super-valent elements at the Zr-site facilitates the vacancies at Li-sites, which stabilizes the highly lithium-ion conducting cubic phase in Li-stuffed garnet with the composition of $Li_7La_3Zr_2O_{12}$ [34-44].

In this study, a Li-garnet $Li_7La_3Zr_2O_{12}$-based cubic $Li_{6.55}La_3Zr_{1.55}Ta_{0.45}O_{12}$ [LLZTO] was synthesized at 900 ºC, exhibiting a bulk ionic conductivity of approximately 6.1×10^{-4} S cm^{-1}. Solid composite electrolytes (SCEs) based on polyethylene oxide (PEO) with different weight fractions of LLZTO powders, acting as bifunctional plasticizers, were fabricated. The high Li^+ conducting LLZTO fillers (i) reduce the crystallinity of the polymer matrix much like the passive fillers (SiO_2, Al_2O_3, etc.) and (ii) provide additional lithium-ion conduction pathways through the ceramic particles. As a result, the highest ionic conductivity of around 2.4×10^{-4} S cm^{-1} at 25 °C was determined for the SCE sample with 20 wt.% LLZTO ceramic filler. Further, to address the dominant cathode-electrolyte interfacial issue in ASSLBs, a cost-effective and easily scalable coating method was adopted, and the electrochemical performance of the fabricated ASSLBs with lithium metal as the anode and $LiFePO_4$ as the cathode is demonstrated (schematically shown in Figure 1(a)).

2. Material synthesis and characterization methods

2.1. Synthesis of LLZTO

The synthesis of the targeted $Li_{6.55}La_3Zr_{1.55}Ta_{0.45}O_{12}$ composition employed the solid-state reaction method. Stoichiometric quantities of lithium hydroxide (LiOH), lanthanum oxide (La_2O_3), zirconium dioxide (ZrO_2), and tantalum oxide (Ta_2O_5) were measured, with 10 wt.% excess lithium precursors to account for lithium volatilization at elevated synthesis temperatures. The initial precursors underwent thorough mixing in a mortar and pestle for 30 minutes, followed by a 12 hours ball-milling process in ethanol. The resulting mixture was pre-heated at 600 °C for 12 hours, then cooled to room temperature. The preheated powder was calcined at 900 °C with a dwell time of 12 hours. Subsequently, the obtained powder was shaped into cylindrical pellets with a diameter of approximately 10 mm and a thickness of about 1 mm, utilizing a uniaxial pressure of 250 MPa in a hydraulic press. The green pellets were sintered at 1150 °C for 12 hours while covered with the same powder.

2.2. Preparation of solid composite electrolytes (SCEs)

The fabrication of SCE membranes involved the dissolution of polyethylene oxide (PEO) polymer and lithium bis(trifluoromethanesulfonyl)imide (LiTFSI) salt in acetonitrile solvent with a molar ratio of EO: Li ~ 8:1. LLZTO powder was then dispersed into the solution at varying weight percentages (SCEx; x = 0, 10, 20, and 30 wt.% of LLZTO powder as the filler). The resulting viscous mixture was thoroughly stirred, drop-cast onto a petri dish, and subjected to vacuum heating at 50 °C for 36 hours to yield the desired SCE electrolyte membranes.

2.3. Integrated cathode-electrolyte architecture

The cathode slurry was prepared with 85 wt.% $LiFePO_4$ (LFP) powder, 10 wt.% Ketjen black, and 5 wt.% polystyrene-block-poly(ethylene-ran-butylene)-block-polystyrene (SEBS) binder, uniformly mixed in Xylene. This slurry was coated onto aluminum foil, followed by vacuum drying at 80 °C for 12 hours. The integrated cathode-electrolyte assembly was then created monolithically by casting the SCE20 (20 wt.% LLZTO & 80 wt.% PEO-LITFSI) electrolyte slurry using a doctor blade coating desktop machine onto the dried LFP cathode ($LiFePO_4$ loading: ~ 2 mg cm^{-2}), as depicted in Figure 1(a). The integrated cathode-electrolyte assembly was vacuum-dried at 50 °C for 36 hours.

2.4. Cell fabrication

Li|SCE20(S)|$LiFePO_4$, Li|SCEx|Li, and Li|SCEx|SS (stainless steel electrode) cells using CR2032, and pouch-type configurations were assembled by sandwiching a SCE20 film between different sets of electrodes. The solid-state lithium metal cell with LFP as the cathode material, denoted as Li|SCE20(C)|$LiFePO_4$, utilized the integrated cathode-electrolyte architecture. The flexible solid state lithium metal pouch cell has been demonstrated in Figure S1.

2.5. Characterizations

Phase confirmation of LLZTO and SCEx electrolytes was conducted using an Empyrean X-ray diffractometer with Cu-Kα radiation (operating at 40 kV, 200 mA) covering the 2θ range of 10° to 60° with a step size of 0.026º and the Topas (version 6) software was employed to perform Rietveld refinement on the x-ray diffraction (XRD) data [45]. Microstructure assessment of composite electrolyte membranes was performed using a JSM field emission scanning microscope (FESEM, model JEOL-7610+). Fourier transform infrared (FTIR) data was obtained within the 500 – 2000 cm^{-1} range using a Perkin Almer Spectrum IR (Model number: Spectrum 2). A PerkinElmer Simultaneous Thermal Analyzer instrument (model number: STA8000) was employed for differential scanning calorimeter (DSC) test and thermogravimetric analysis (TGA) of SCE0 and SCE20 electrolyte samples at a heating rate of 10 °C min^{-1}. Impedance Measurements were conducted on various cells and pellets using an NF LCR meter (Model: ZM2376) with a 10 mV perturbation signal. A Keithley Source Meter Unit (model 2450-EC) was employed for linear sweep voltammetry (LSV) in Li|SCEx|SS with Li-electrodes and stainless-steel (SS) electrodes at 25 ºC (RT) in a 2.5-5.5 V range at a scan rate of 0.1 mV s^{-1}. Room temperature galvanostatic charge-discharge tests were conducted on Li|SCEx|Li, Li|SCE20(C)|$LiFePO_4$, and Li|SCE20(S)|$LiFePO_4$ cells in Neware battery tester (Model no. CT-4008T).

3. Results and discussion

3.1. XRD analysis

Figure 1(b) shows the XRD pattern of LLZTO calcined at 900 ºC for 12 h with a heating rate of 5 ºC min^{-1}. The Rietveld refinement performed using TOPAS software (academic version) confirmed the cubic phase (space group: $Ia\overline{3}d$) with a lattice parameter a = 12.9678(7) Å and V = 2180.715(4) Å^3 [45]. During Rietveld refinement, both the tetragonal and cubic structures were taken as the starting models, and the refinement results are provided in Table 1. The refinement results confirmed the pure cubic phase with partial substitution of Ta^{5+} at Zr^{4+} sites. Two Wyckoff sites [24d site, distorted 96h site] are available for the random distribution of lithium ions in the cubic Garnet phase. A disorder in Li distribution driven by

Li vacancy concentration (0.4-0.5 atoms per formula unit) is required to reduce the Li-Li repulsion for stabilization of the cubic phase in lithium-stuffed garnet electrolytes ($Li_7La_3Zr_2O_{12}$) [46]. 22.5% Zr^{4+} substitution by Ta^{5+} in $Li_7La_3Zr_2O_{12}$ creates 0.45 Li vacancy per formula unit, which is sufficient to prevent the transformation of the cubic phase to the tetragonal phase at room temperature.

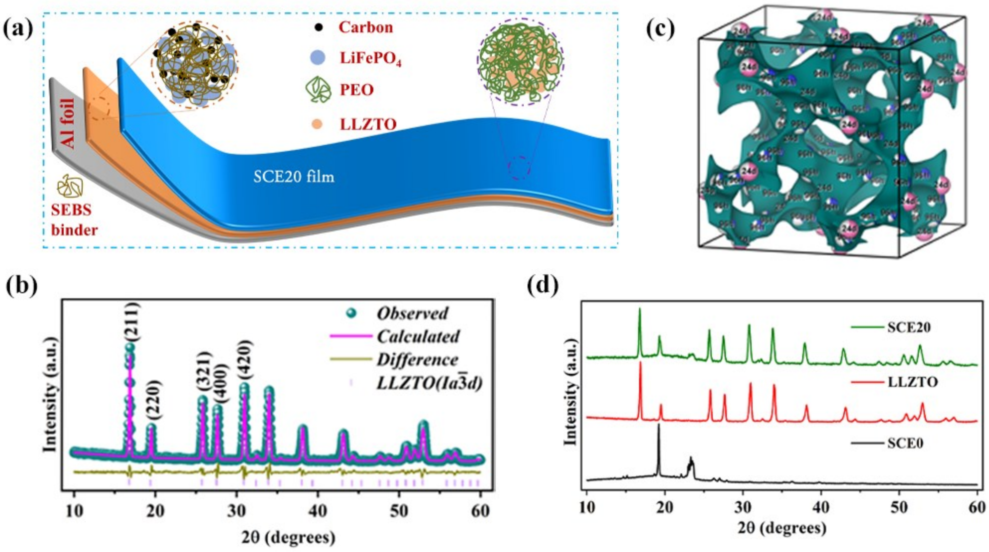

Figure 1. (a) Schematic illustration of integrated cathode-electrolyte architecture using a doctor blade. (b) Room temperature powder x-ray diffraction data (closed dark cyan spheres) for $Li_{6.55}La_3Zr_{1.55}Ta_{0.45}O_{12}$ *(LLZTO) sample calcined at 900 °C for 12 h. The calculated pattern obtained from the refinement is shown as a thick magenta line; the profile difference is depicted with a thin dark yellow line. The calculated Bragg positions for LLZTO are shown by thin magenta vertical bars at the bottom. (c) Lithium-ion migration pathway in the cubic LLZTO(*$Ia\bar{3}d$*) crystal generated using softBV software. (d) Room temperature XRD patterns of SCE0, LLZTO ceramic powder, and SCE20 composite electrolyte.*

As reported, the neutron powder diffraction studies have confirmed a decrease in the Li occupancy at the tetrahedral 24d site and an increase in occupancy at the octahedral 96h site upon an increment in lithium concentration in the range of 5-6.6 per formula unit [47]. Further, the partial vacancy at the distorted octahedral 96h site is vital in achieving an easier Li^+ transport channel in the crystal structure. For the Li^+ conduction pathways in LLZTO, bond valence site energy (BVSE) calculations are executed utilizing the softBV software developed by Adams' group [48, 49]. The energy assessments for different lithium sites within the LLZTO solid electrolyte crystal structure are computed across 3D point grids at 0.1 Å resolution. This is achieved utilizing the transferable Morse-type softBV force field. The BVSE maps, delineating constant iso-surface energy at low energy sites (Li^+), determine the favored Li-ion diffusion route within the crystal lattice of LLZTO electrolyte. The Vesta file generated from the software corresponding to the cubic LLZTO CIF file was used to visualize the lithium-ion migration pathway in our LLZTO electrolyte crystal structure (Figure 1(c)) [50]. Li^+ migration occurs through both 24d and 96h sites in the crystal.

Table 1. *Results from Rietveld refinement of room temperature powder XRD data of* $Li_{6.55}La_3Zr_{1.55}Ta_{0.45}O_{12}$.

Site	***Wyckoff position***	***x***	***y***	***z***	***Atom***	***Occupancy***
Li1	24d	0	0.75	0.625	Li^{+1}	0.657
Li2	96h	0.43(3)	0.08(2)	0.20(3)	Li^{+1}	0.381
La	24c	0.125	0	0.25	La^{+3}	1
Zr	16a	0	0	0	Zr^{+4}	0.775
Ta	16a	0	0	0	Ta^{+5}	0.225
O	96h	0.291(4)	0	0.25	O^{-2}	1

In Figure 1(d), the peak at ~ 23.4° is of low intensity and broad in the XRD pattern of SCE20, demonstrating that the introduction of LLZTO might decrease the crystallinity of PEO-LiTFSI. This reduction in crystallinity promotes the facile migration of lithium ions within the polymer chain. Further, the characteristic peaks of cubic LLZTO affirmed the ceramic-polymer compatibility.

3.2. FTIR analysis

FTIR analysis was utilized to examine the polymer's stability and determine whether the incorporation of a ceramic filler had a noteworthy impact on structural alterations within the polymeric matrix. Figure 2(a) presents the FTIR spectra of PEO, SCE0, and SCE20 samples in the 400-2000 cm^{-1} range. The doublet peaks at ~ 1340 cm^{-1} and 1360 cm^{-1} denote the -CH_2 wagging of PEO polymer, whereas the characteristic peaks at ~ 1054 cm^{-1} and 1103 cm^{-1} represent the C-O-C stretching of the PEO [51]. The 964 cm^{-1} and 1466 cm^{-1} peaks represent -CH_2 twisting and -CH_2 asymmetric bending in the PEO polymer [52]. The distinctive vibrations of PEO were detectable both prior to and following the introduction of the Li-salt and LLZO ceramic filler. Upon the addition of LiTFSI salt, the peak at ~ 1360 cm^{-1} shifted towards a lower wavelength, and where in SCE20, there is a blue shift of peaks at ~ 1360 cm^{-1} and 1340 cm^{-1}. The peaks at ~ 762 cm^{-1} and ~ 737 cm^{-1} denote the Li^+-$TFSI^-$ contact pairs and free $TFSI^-$ respectively, in the FTIR spectra of both SCE0 and SCE20 FTIR spectra [53, 54]. The slight decrease in the area of the peaks indicated the increase in the number of free lithium ions in the SCE20 electrolyte membrane. Further, the peak shift due to the addition of LLZTO indicates the Lewis acid-base interaction between the ceramic particles and $TFSI^-$.

3.3. Microstructure analysis

Figure 2(b1) presents the EDS mapping of SCE20, and Figure 2(b2-b8) shows the elemental distributions of S, O, C, F, La, Ta, and Zr.

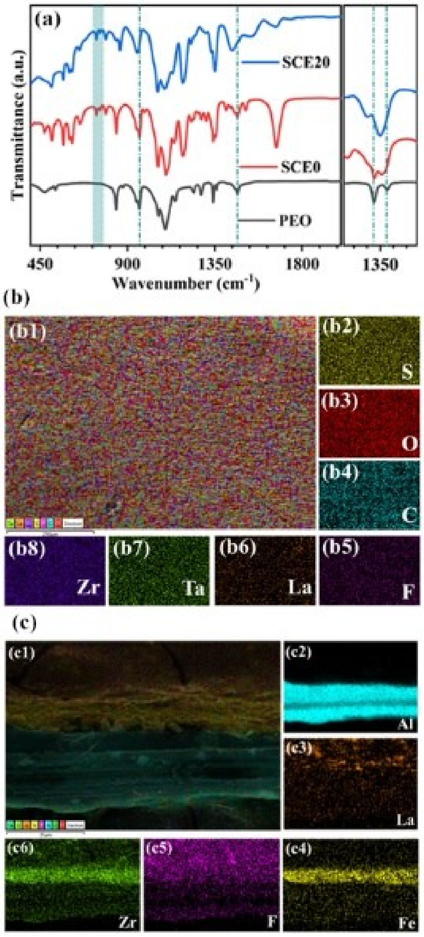

Figure 2. (a) FTIR spectra of PEO, SCE0, and SCE20 samples, (b) EDS mapping of SCE20 electrolyte (b1) along with elemental distributions of S, O, C, F, La, Ta, and Zr (b2-b8). (c) EDS mapping of a cross-section of the SCE20-LiFePO$_4$ assembly (c1) along with elemental distributions of Al, La, Fe, F, and Zr (c2-c6).

The well-connected polymer matrix contains uniformly dispersed ceramic particles, which can be conducive to the lower activation energy of lithium-ion migration in the composite electrolyte. Figure 2(c1) demonstrates a cross-sectional EDS mapping of the electrolyte (SCE20) coated on the cathode (LFP) along with the elemental distributions of Al, La, Fe, F, and Zr (c2-c6). An intimate contact between the cathode and electrolyte surface was found without visible delamination. EDS mapping of La and F confirmed the infusion of SCE20 electrolytes into the cathode. As-dried coated-cathode sheet is porous, the electrolyte slurry (PEO/LiTFSI + acetonitrile + LLZTO) infiltrates these pores, providing a tortuous interface between cathode and SCE. The binding force between the cathode and electrolyte is believed to be arising from the minimization of surface free energy.

The insolubility of SEBS binder (in polar solvents like acetonitrile) used for LFP coating helped in maintaining the integrity of the LFP layer and its adhesion to the current collector while casting the electrolyte slurry on top of the cathode, evidenced by the elemental mapping of Al and Fe given in Figure 2(c2) & 2(c4). On the cathode side, lithium-ion conductive channels are provided by the incorporated SCE20 electrolyte into the pores in the LFP cathode, which is expected to enhance the electrochemical performance of the full cell fabricated by monolithic cathode-electrolyte construction.

3.4. Thermal analysis

Figures S3 and S4 demonstrate thermogravimetric analysis (TGA) and differential scanning calorimeter (DSC) data of SCE0 and SCE20 composite electrolytes, respectively. In Figure S2, the decomposition of PEO polymer started at ~ 300 °C, and the SCE20 electrolyte has a higher retention of mass as compared to that of SCE0, as 20 wt.% LLZTO is present in the SCE20 sample. DSC data also revealed that the melting temperature reduced slightly from ~ 57 °C to ~ 52 °C upon incorporation of 20 wt.% ceramic fillers, along with a decrease in the area of the melting peak, confirming a decrease in the degree of crystallinity of SCE0 electrolytes.

3.5. Complex impedance analysis

The sintered LLZTO electrolyte surfaces were painted uniformly with silver (Ag) electrodes, and the solid composite electrolytes (SCEx) were sandwiched between two stainless steel spacers to measure their impedance responses under a 10 mV perturbation across a wide range of frequencies (1 Hz – 1 MHz) at different temperatures. Figure 3(a) shows the room temperature Nyquist plots of LLZTO, along with corresponding equivalent circuit used for data fitting as the figure inset. For the LLZTO sample, the presence of a straight line at the low-frequency end in the Nyquist plot denotes the ionic polarisation at the Ag electrode surface, whereas the data fitting confirmed the presence of grain resistance (R_g) and grain boundary relaxation ($CPE1||R_{gb}$) in the high and mid-frequency regime, respectively. The bulk(grain) conductivity and total conductivity of the LLZTO sample were calculated to be ~ 6.1×10^{-4} S cm^{-1} and ~ 1.83×10^{-4} S cm^{-1} using the dimensions of the sample and fitted value of the resistances. Although the use of sintered LLZTO alone in the solid-state battery was hindered by high resistance and poor densification, its bulk conductivity enabled its use as an active lithium-ion conductive filler in the PEO/LiTFSI polymer matrix. The bulk conductivities of LLZTO electrolytes at different temperatures were used to determine the activation energy by linear fitting of conductivity values using the Arrhenius equation as given by:

$$\sigma(T) = \sigma_0 e^{\left(\frac{-E_a}{k_B T}\right)} \tag{1}$$

wherein T, E_a, and σ_0 denote the absolute temperature, activation energy, and pre-exponetial factor, respectively (Figure 3(b)). The high conductivity of ~ 6.1×10^{-4} S cm^{-1} at room temperature and low activation energy of ~ 0.379 ± 0.007 eV can be attributed to the concerted lithium-ion migration through the distorted tetrahedral sites (96h) in the cubic lattice stabilized by partial Ta^{5+} substitution at the Zr-site.

In the Nyquist plot of SCE20 (Figure 3(c)), one tail feature (CPE2) at the low-frequency region denotes the ion-blocking nature of the stainless steel along with a partial semicircle (R||CPE1) at the high-frequency regime symbolizing the lithium-ion percolation inside the composite electrolyte. The fitted ‘R’ value, along with the thickness and the surface area, were used to calculate the conductivity values of the composite electrolyte samples.

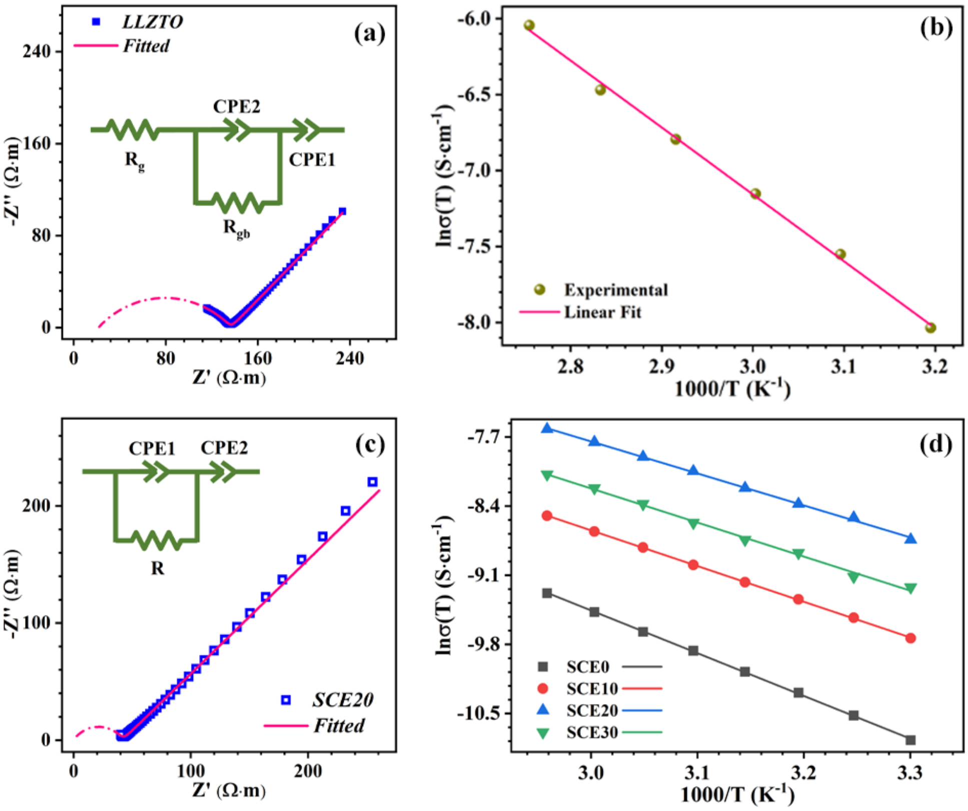

Figure 3. (a) Room temperature Nyquist plot of LLZTO (inset displays the equivalent circuit used for fitting the impedance data). The dotted line indicates the extrapolated data using simulation. (b) Linear fitting of temperature-dependent conductivities of LLZTO using the Arrhenius equation. (c) Room temperature Nyquist plot of SCE20 (inset displays the equivalent circuit used for fitting the impedance data). The dotted line indicates the extrapolated data using simulation. (d) Linear fitting of temperature-dependent conductivities using the Arrhenius equation for SCEx (x = 0, 10, 20, and 30) samples.

Figure 3(d) shows the linear fitting of conductivities of SCEx at different temperatures using equation (1). The activation energy and room temperature total conductivity value of SCEx are given in Table 2. The SCE20 sample showed the highest conductivity of ~ 2.4 × 10^{-4} S cm^{-1} and the lowest activation energy for lithium-ion transport of ~ 0.278 ± 0.005 eV amongst SCEx (x = 0, 10, 20, and 30) samples. It is known that incorporating lithium-ion conducting ceramic powders in polymers diminishes the polymer matrix's semi-crystalline nature and provides additional conduction channels either through the ceramic grains or space charge region formed at the ceramic-polymer interface, thereby enhancing lithium-ion conduction [55]. The lower conductivity and higher activation energy of SCE30 compared to the SCE20 sample could be due to the aggregation of LLZTO particles, as shown in Figure S2.

Table 2. *Room temperature total conductivity, activation energy, and lithium-ion transference number (t_{Li+}) of SCEx.*

Sample	**Total conductivity at RT (S cm^{-1})**	**Activation energy (eV)**	**t_{Li+}**
SCE0	0.59 × 10^{-4}	0.372 ± 0.002	0.30(5)
SCE10	1.3 × 10^{-4}	0.311 ± 0.001	0.36(4)
SCE20	2.4 × 10^{-4}	0.278 ± 0.004	0.61(3)
SCE30	1.8 × 10^{-4}	0.297 ± 0.007	0.45(9)

3.6. Lithium-ion transference number

The lithium dendrite formation and coulombic efficiency at higher C-rates are partially influenced by the lithium-ion transference number, where a localized electric field develops at the electrode surface due to an uneven concentration of anions and cations. The Bruce-Vincent technique, integrating both direct current (DC) and alternating current (AC) measurement methods, is commonly used to estimate the Li^+ transference number [56]. For the measurement of Li^+ transference numbers using the Bruce-Vincent technique at 25 °C, a 100 mV DC potential (ΔV) was applied across symmetric Li|SCEx|Li cells for 3 h, after which no significant change in current was observed. The impedance of the symmetric cell was measured using a 10 mV AC perturbation before the application of DC potential to determine the interfacial resistance of the cell. Upon the DC potential application, both the cationic and anionic species contribute to the initial current value (I_0) at t = 0 h. With time, there was a decline in the current value due to a reduction of the anionic current as the anions were blocked at the lithium metal electrode's surface and the developed counter-electric field in the direction opposite of the applied DC field. At the steady state (t = 3 h), the current (I_{ss}) was only due to the migration of the cationic species through the electrolyte. Again, the interfacial resistance at steady state (I_{ss}) was determined through EIS measurements. Figure 4(a) depicts the current variation in Li|SCE20|Li cells subjected under 100 mV DC potential over 3 hours, and the inset presents Nyquist plots Li|SCE20|Li cells measured at t = 0 h and t = 3 h. Impedance data was fitted using an equivalent circuit (Figure 4(a) inset). The high-frequency intercept of the semi-circular arc corresponds to the composite electrolyte resistance, while the low-frequency intercept provides the total resistance of the symmetric cell. The interfacial resistance, obtained by the difference between these two resistances, increased from 200 Ω to 213 Ω after DC polarization, while the bulk resistance of the SCE20 electrolyte remained relatively unchanged. The t_{Li+} values for SCEx are calculated using equation (2) and presented in Table 2.

$$t_{Li^+} = \frac{I_{ss}(\Delta V - I_0 R_0)}{I_0(\Delta V - I_{ss} R_{ss})} \tag{2}$$

There is always a trade-off between ionic conductivity and lithium-ion transference number in the case of liquid electrolytes, but ceramic incorporation in the polymer electrolytes improves both the lithium-ion conductivity and lithium-ion transference number. The sample with a 20 wt.% ceramic content (SCE20) exhibited the maximum t_{Li+} of approximately 0.61, aligning with the trend observed in ionic conductivity. Inorganic lithium-ion conductive ceramics are known for their high Li-ion transference numbers, often nearing 1. Incorporating Li-stuffed Garnet fillers restricts the motion of $(TFSI)^{-}$ and poly-ions, contributing to the elevated Li-ion transference number in the SCE20 composite compared to the SCE0 sample with t_{Li+} ~ 0.30. Additionally, LLZTO particles may act as Lewis acid sites, facilitating complexation between the anion part of LiTFSI salt and t_{Li+}, thereby increasing the Li^{+} transference number. However, SCE30 exhibited a decrease in t_{Li+} compared to SCE20, which might result from LLZTO particle aggregation. Figure 4(b) demonstrates the effective room lithium-ion conductivity of LLZTO and SCEx samples considering both ionic conductivity and lithium-ion transference number at room temperature. The SCE20 electrolyte was found to have the highest lithium-ion conductivity of ~ 1.64×10^{-4} S cm^{-1} amongst SCEx samples.

Figure 4(c) exhibits the results of the linear sweep voltammetry tests carried out on Li|SCE0|SS cell and Li|SCE20|SS cell within a 2.5-5.5 V range at a scan rate of 0.1 mV s^{-1}. The sudden exponential current increase at a particular voltage is caused by the oxidation of the electrolyte (irreversible side reactions), determining the upper cut-off voltage of the operation lithium cell. In the Li|SCE0|SS cell, the onset of rapid increase in current is ~ 4.5 V, while a higher onset voltage of ~ 5.1 V was observed in the Li|SCE20|SS cell. The Lewis acid-base interaction of LLZTO particles with the functional groups in the PEO-LiTFSI matrix improved the electrochemical stability. Determining the oxidation stability by setting a limiting current value of ~ 10 μA would also suggest the enhanced oxidation stability of the SCE20 electrolyte upon the impregnation of LLZTO particles in the SCE0 electrolyte.

Overall, the high oxidation stability of SCE20 electrolyte bestows the use of high-voltage spinel-type cathodes, layer oxides, etc., in ASSLBs.

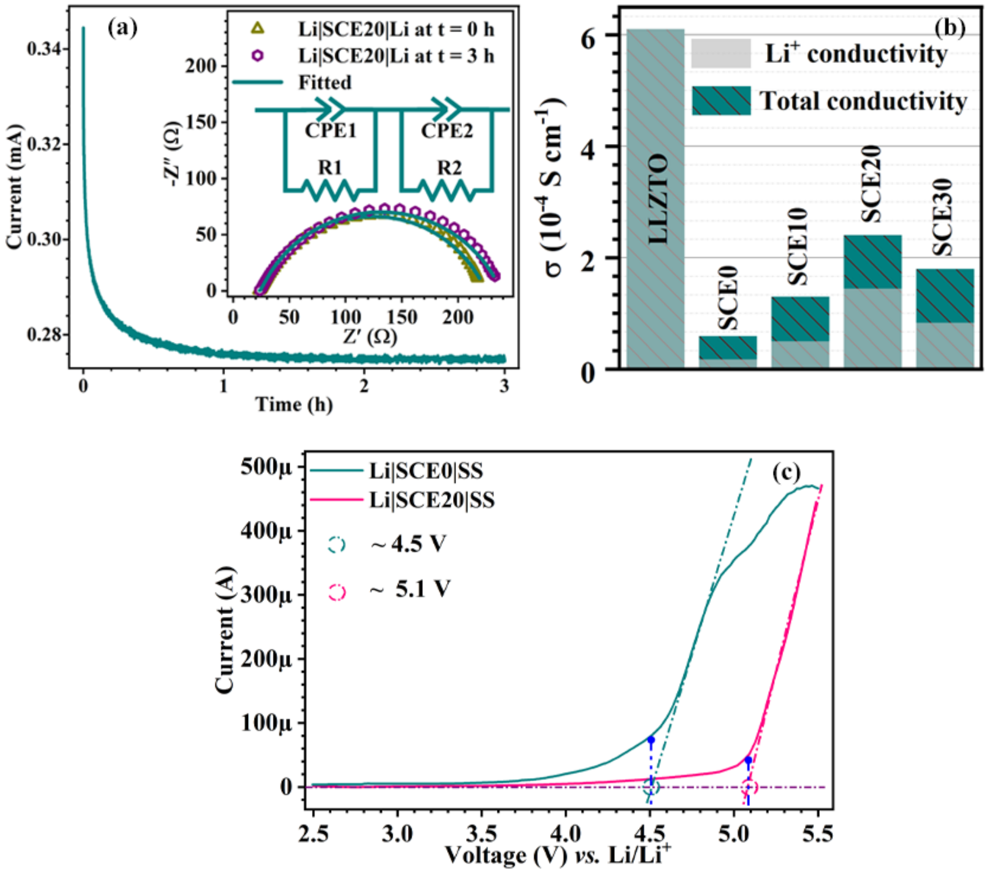

Figure 4. (a) Current variation with time upon applying 0.1 V on symmetric Li|SCE20|Li cell at room temperature. The inset shows the Nyquist plots at t = 0 h & t = 3 h with the appropriate equivalent circuit used to fit the data. (b) The histogram presents the room-temperature lithium-ion conductivity and total conductivity of LLZTO and SCEx (x= 0, 10, 20, and 30). (c) Linear sweep voltammetry curves for Li|SCE0|SS cell and Li|SCE20|SS cell at 0.1 mV s^{-1} at room temperature.

3.7. Symmetric cell GCD

The room temperature cycling performance of Li symmetric cells employing SCE20 membranes was investigated to assess the interfacial stability and compatibility of the electrolyte with the lithium metal electrode. Figure 5(a) illustrates the galvanostatic charge-discharge (GCD) profiles of lithium symmetric cells (with SCE20 as the electrolyte) at various current densities (0.1 mA cm^{-2}, 0.2 mA cm^{-2}, 0.4 mA cm^{-2}, 0.6 mA cm^{-2}, and 0.8 mA cm^{-2}) for 30 minutes of lithium plating and 30 minutes of stripping. With the increase in the areal current density up to 0.6 mA cm^{-2}, the flatness in the overpotential profile gradually decreases along with increased overpotential values. At 0.8 mA cm^{-2}, the sign of micro short-circuit was evident from the erratic voltage profile. Considering the presence of electrical integrity up to 0.6 mA cm^{-2}, the critical density of the SCE20 electrolyte was determined to be ~ 0.6 mA cm^{-2}. At a high areal current density of 0.4 mA cm^{-2}, the lithium symmetric cell employing SCE20 not only showed ~ 180 mV overpotential at the end of charging and discharging but also exhibited long cycling durability of more than 1100 cycles of lithium plating and stripping without any sign of micro short circuit or complete short circuit (Figure 5(b)). There was an increase in the overpotential value to ~ 320 mV after 800 cycles, which remained almost constant upon further cycling, suggesting the stable interface formation between lithium metal and SCE20 electrolyte. Further, the symmetric cell overpotential curve during charging and discharging indicated uniform lithium deposition and stripping from the lithium metal surface [57].

To showcase the robustness and viability of SCE20 compared to SCE0 electrolyte, the Galvanostatic Charge-Discharge (GCD) plots of the Li|SCE0|Li cell at a current density of 0.1 mA cm^{-2} are illustrated in Figure 5(c). Notably, the symmetric cell with SCE0 exhibits larger over-potentials compared to its SCE20 counterpart at a current density of 0.1 mA cm^{-2} and the overpotential increased with cycling. The increasing overpotential suggested the unstable SEI formation at the lithium metal-SCE0 interface. After cycling for 80 hours, there was a sudden spike in the overpotential, denoting the torturous lithium transport path through dead lithium due to inhomogeneous lithium deposition at the lithium metal, but in the next cycles, the decrease in the overpotential suggested the micro short-circuit through the SCE0 electrolyte. Although there was no complete short-circuit, the electronic migration through the SCE0 electrolyte was evinced by the flat potential curves shown in the mustard color in Figure 5(c) inset. The electronic conduction in the electrolyte through micro dendrites is detrimental in full-cell operations, causing low coulombic efficiency and complete lithium dendrite penetration through the electrolyte, shorting the cell to zero potential.

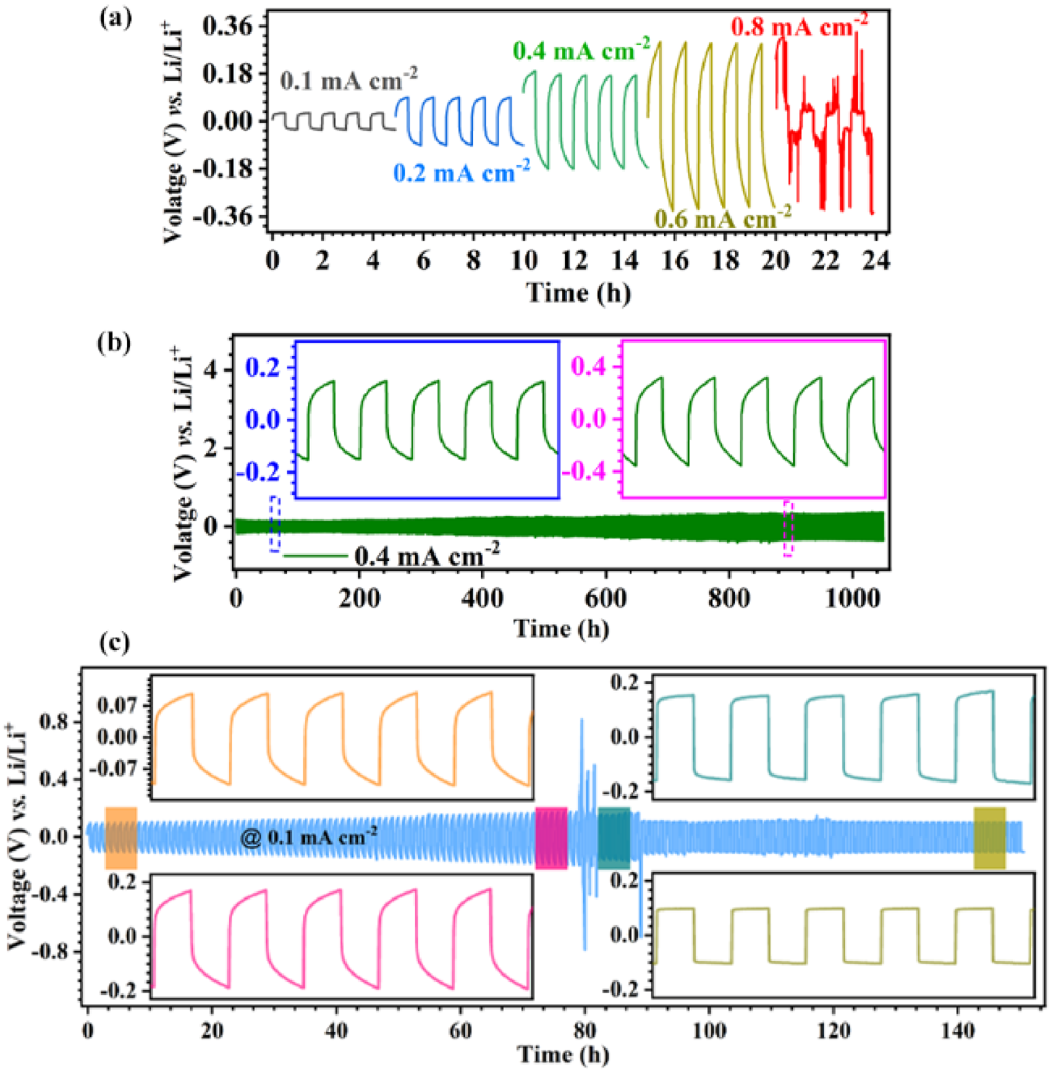

Figure 5. (a) The galvanostatic charge-discharge data of Li|SCE20|Li cell at different current densities at room temperature. (b) The galvanostatic charge-discharge data of Li|SCE20|Li cell at 0.4 mA cm^{-2} for 1100 h at room temperature. (c) The galvanostatic charge-discharge data of Li|SCE0|Li cell at 0.1 mA cm^{-2} at room temperature.

3.8. Full cell performance

Figure 6(a) depicts the specific capacity-potential curves of Li|SCE20(S)|$LiFePO_4$ cells at different C-rates (the C-rates are calculated using the theoretical specific capacity of $LiFePO_4$ ~ 170 mAh g^{-1}). At 0.2C, the full Li|SCE20(S)|$LiFePO_4$ cell (SCE20 electrolyte membrane stacked between Li metal and $LiFePO_4$) delivered a specific capacity of ~ 127 mAh g^{-1} with a polarization potential of ~ 460 mV at 50% state of charge (SOC). With the increase in the C-rate, there is a decrease in the specific capacity accompanied by an elevation in the polarization potentials. At 0.5C and 1C, the specific capacity decreased to ~ 107 mAh g^{-1} and ~ 70 mAh g^{-1}, respectively, with higher polarization potentials at 50% SOC of ~ 521 mV and 845 mV. The poor rate performance may be attributed to the sluggish lithium-ion transport kinetics on the cathode side and the imperfect solid-solid electrolyte-cathode interface.

Figure 6(b) demonstrates the galvanostatic charge-discharge voltage profile of the Li|SCE20(C)|$LiFePO_4$ cell fabricated by a monolithic cathode-electrolyte interface design at different C-rates. A high specific capacity of ~ 157 mAh g^{-1} at 0.2C was obtained with a very low polarization potential of ~ 120 mV compared to its counterpart cell Li|SCE20(S)|$LiFePO_4$, as discussed above. The specific capacity decreased to ~ 150 mAh g^{-1} at 0.5C, ~ 133 mAh g^{-1} at 1C, and ~ 100 mAh g^{-1} at 2C, along with increased polarization potential driven by Li^+ transport kinetics inside the cell. The improved rate performance is due to the conversion of the $LiFePO_4$ cathode into a $LiFePO_4$/SCE20 catholyte as the infused electrolyte into the cathode side filled the space between the $LiFePO_4$ particles, providing the facile Li^+ transport channels, thus enhancing the number of $LiFePO_4$ particle's participation in the charge-discharge electrochemistry. There is a lower change in the specific capacities and a lower difference in polarization potentials at 0.2C and 0.5C compared to 1C and 2C, respectively. This may be attributed to the low lithium-ion diffusion coefficient (~ 10^{-14} cm^2 s^{-1}) and poor electronic conductivity (~ 10^{-9} S cm^{-1}) of the $LiFePO_4$ electrode [58, 59].

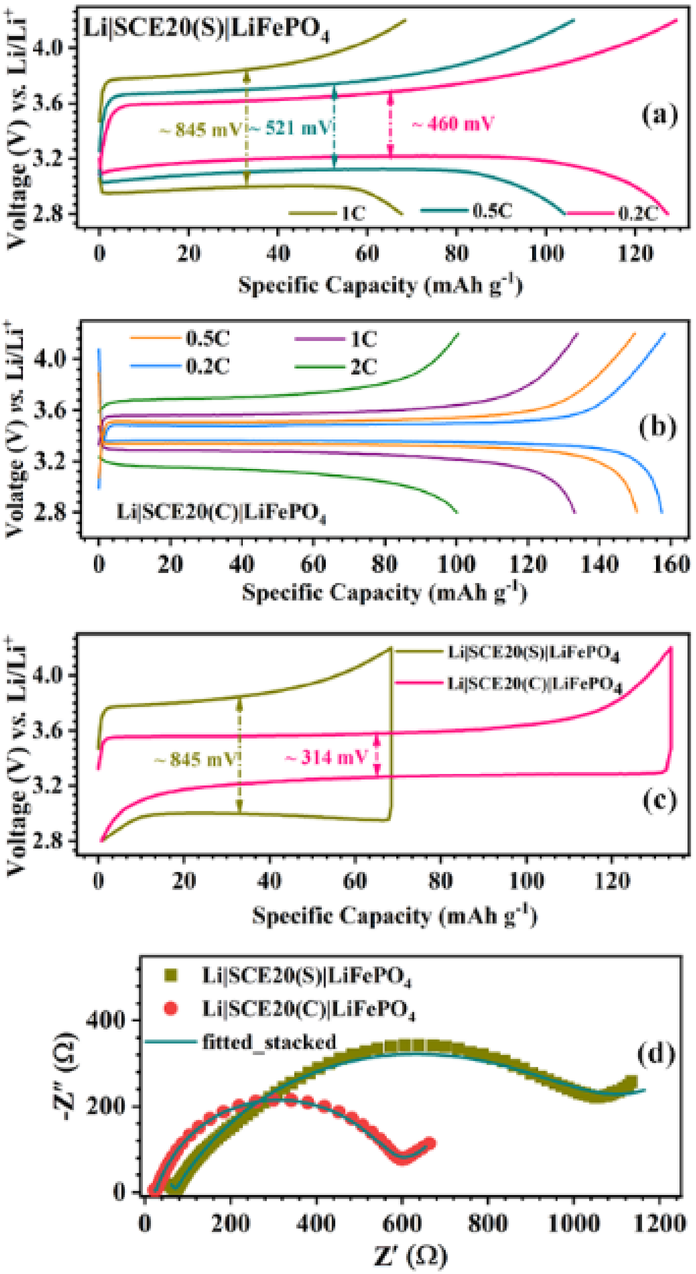

Figure 6. The specific capacity-potential curves of (a) Li|SCE20(S)|LiFePO$_4$ and (b) Li|SCE20(C)|LiFePO$_4$ cells at different C-rates at room temperature. (c) The comparison of voltage vs. specific capacity curves of Li|SCE20(S)|LiFePO$_4$ and Li|SCE20(C)|LiFePO$_4$ cells at 1C. (d) The room temperature Nyquist plots of Li|SCE20(S)|LiFePO$_4$ and Li|SCE20(C)|LiFePO$_4$ at 50% state of charge.

Figure 6(c) presents the voltage *vs.* specific capacity plot of Li|SCE20(S)|$LiFePO_4$ and Li|SCE20(C)|$LiFePO_4$ cells at 1C. There is a ~ 63% decrease in the polarization potential value upon employing the integrated electrode-electrolyte architecture to fabricate the cells. Figure 6(d) shows the Nyquist plots of Li|SCE20(S)|$LiFePO_4$ and Li|SCE20(C)|$LiFePO_4$ cells in a frequency range of 1 Hz - 1 MHz with a perturbation voltage of 10 mV. There is a clear decline in the charge transfer resistance (total resistance – electrolyte resistance) of the Li|SCE20(C)|$LiFePO_4$ cell due to the better cathode-electrolyte interface design as compared to the Li|SCE20(S)|$LiFePO_4$ cell. The decreased charge transfer resistance can be attributed to the intimate electrode-electrolyte interface contact and the improved Li^+ transport kinetics provided by the SCE20 electrolyte filled in the porous cathode side, as illustrated by the schematic in Figure 1(a). The 50% lower cell resistance obtained from the EIS data corroborates the lower polarization potential observed in the Li|SCE20(C)|$LiFePO_4$ cell at 0.2C as compared to the Li|SCE20(S)|$LiFePO_4$ cell.

Figure 7(a) shows the long cycling galvanostatic charge-discharge performance of Li|SCE20(C)|$LiFePO_4$ cell at 1C for 1000 cycles. The coulombic efficiency was less than 99% in initial cycles, which improved on cycling and remained thereafter at ~ 100% during the charging-discharging process over 1000 cycles. Coulombic efficiency plays a vital role in commercial applications from the lithium dendrite growth and capacity fading perspective. The high coulombic efficiency indicates the electrolyte's very low intrinsic electronic conductivity and the absence of any micro short circuit driven by irregular lithium dendrite growth through the electrolyte membrane. The Li|SCE20(C)|$LiFePO_4$ cell sustained 1000 cycles of charge-discharge at 1C with a capacity retention of ~ 84.2% of the initial discharge capacity of ~ 133 mAh g^{-1}. To demonstrate the impact of integrated cathode-electrolyte architecture on cell performance, the long-term cycling data of Li|SCE20(S)|$LiFePO_4$ cell is shown in Figure 7(b). The Li|SCE20(S)|$LiFePO_4$ cell delivered an initial specific capacity of

~ 67 mAh g^{-1} and retained only ~ 36% capacity after 300 cycles. Further, a comparison of studies with the same cathode-anode chemistries using composite electrolytes (LiFePO4: cathode, lithium metal: anode), including this work, is provided in Table S1. The capacity loss is attributed to the unavoidable irreversible chemical reactions at the electrodes-electrolyte interface and the continuous lattice breathing of the cathode particles during charge-discharge cycles. Figure 7(c) demonstrates the representative capacity-potential curves for different cycles at 1C for 1000 cycles. The gradual upward shift of nominal charging voltage and the downward shift of nominal discharging voltage indicate a decrease in energy efficiency. The increase in the difference between charging and discharging nominal voltages can be due to the elevated total cell resistance dominated by the electrode-electrolyte interfacial resistance, as illustrated in Figure 7(d). There was a 75% increase in the electrode-electrolyte interfacial resistance from ~ 600 Ω at 1st cycle to ~ 1050 Ω at the 1000th cycle at 1C. Thus, further improvement in the interface chemistry is needed to minimize the percentage increase of the cell resistance upon cycling to get enhanced cyclability with minimum energy loss per cycle. The pouch cell also demonstrated its ability to function under external bending stresses, as shown in Video S1.

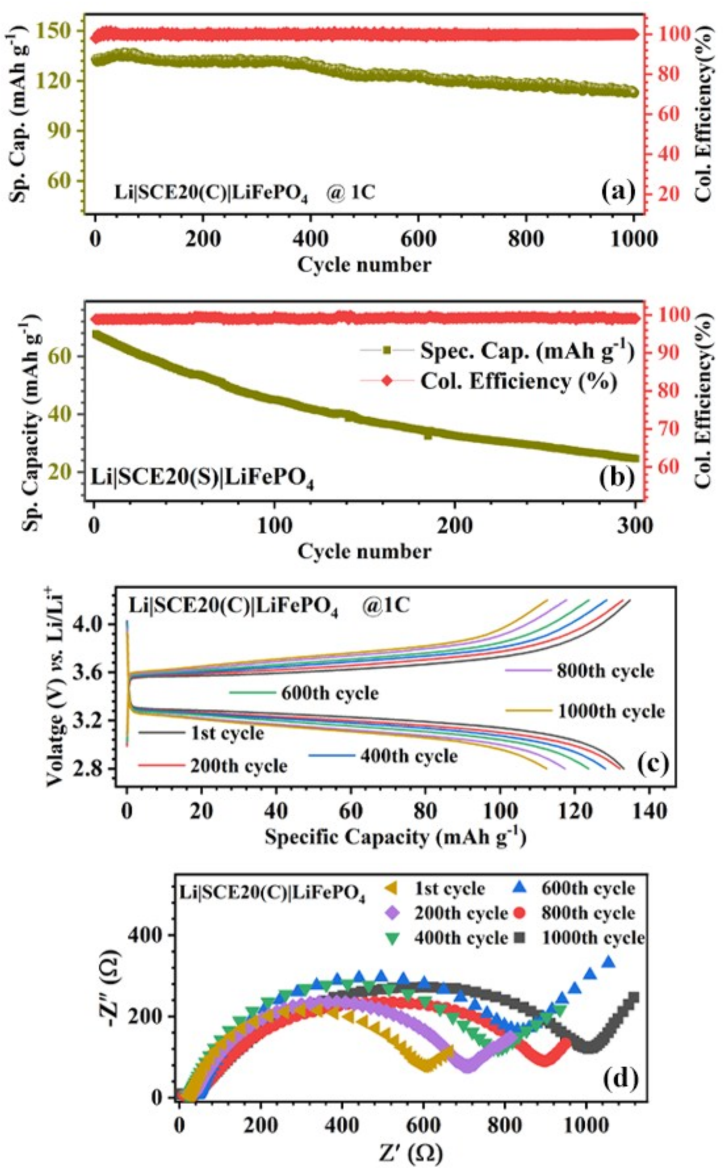

Figure 7. Room temperature long cycling data show discharge specific capacity and columbic efficiency of (a) Li|SCE20(C)|LiFePO$_4$ cell & (b) Li|SCE20(C)|LiFePO$_4$ cell at 1C. (c) Room temperature galvanostatic charge-discharge specific capacity-voltage curves of Li|SCE20(C)|LiFePO$_4$ cell at 1C (1st, 200th, 400th, 600th, 800th, and 1000th cycle). (d) Room temperature Nyquist plots of Li|SCE20(C)|LiFePO$_4$ cell during 1st, 200th, 400th, 600th, 800th, and 1000th cycle at 50% SOC.

4. Conclusions

The solid composite electrolyte sample containing 20 wt.% cubic LLZTO (Space group: $Ia\bar{3}d$, grain conductivity: ~ 6.1×10^{-4} S cm^{-1}) ceramic powders demonstrated superior characteristics, including the highest room temperature ionic conductivity (~ 2.4×10^{-4} S cm^{-1}), the lowest activation energy (~ 0.278 ± 0.005 eV), and the highest lithium-ion transference number (~ 0.61) among all SCEx samples. The galvanostatic charge-discharge (GCD) data of the Li|SCE20|Li cell over 1100 cycles showcased its durability and long-cycle stability, maintaining an overpotential of approximately 180 mV at a current density of 0.4 mA cm^{-2} with a critical current density of ~ 0.6 mA cm^{-2}. The full Li|SCE20(C)|$LiFePO_4$ cell, when fabricated using a monolithic electrode-electrolyte integrated assembly, exhibited an initial discharge capacity of around 133 mAh g^{-1}, retaining approximately ~ 84.2% of its capacity after 1000 cycles at 1C. The enhanced rate performance of Li|SCE20(C)|$LiFePO_4$, compared to Li|SCE20(S)|$LiFePO_4$, highlights the significance of a well-designed electrolyte-cathode interface. The utilization of a simple doctor blade coating technique, combined with appropriate solvent selection for the preparation of cathode-composite solid electrolyte bi-layers, as demonstrated in this study, holds promise for advancing the commercialization of all-solid-state lithium metal batteries.

Author information:

Asish Kumar Das: Conceptualisation, Methodology, Investigation, Funding acquisition, Writing - Original Draft; **Manish Badole:** Data Curation (SEM), Writing - Review & Editing; **Hari Narayanan Vasavan:** Data Curation (XRD), Writing - Review & Editing; **Samriddhi Saxena:** Writing - Review & Editing; **Pratiksha Gami:** Writing - Review & Editing; **Neha Dagar:** Writing - Review & Editing; **Sunil Kumar:** Conceptualisation, Methodology, Funding acquisition, Supervision, Resources, Project administration, Validation, Writing - Review & Editing.

Declaration of competing interest:

There are no conflicts to declare.

Data availability:

Data will be made available on request.

Acknowledgements:

The author (AKD) thanks the Ministry of Education, Government of India, for the Prime Ministers Research Fellowship (PMRF) (PMRF ID - 2102737). The authors gratefully acknowledge the Science and Engineering Research Board (SERB), Government of India (Grant No. CRG/2021/005548) and Department of Science and Technology (DST), Government of India (Grant No. DST/TMD/IC-MAP/2K20/01).

References

[1] M. Winter, B. Barnett, K. Xu, Before Li Ion Batteries, Chem. Rev., 118 (2018) 11433 https://doi.org/10.1021/acs.chemrev.8b00422

[2] B. Diouf, R. Pode, Potential of lithium-ion batteries in renewable energy, Renew. Energ., 76 (2015) 375 https://doi.org/10.1016/j.renene.2014.11.058

[3] H.N. Vasavan, M. Badole, S. Saxena, A.K. Das, S. Deswal, P. Kumar, S. Kumar, Excellent Structural Stability-Driven Cyclability in P2-Type Ti-Based Cathode for Na-Ion Batteries, ACS Appl. Energy Mater., 6 (2023) 2440 https://doi.org/10.1021/acsaem.2c03750

[4] S. Saxena, H.N. Vasavan, M. Badole, A.K. Das, S. Deswal, P. Kumar, S. Kumar, Tailored P2/O3 phase-dependent electrochemical behavior of Mn-based cathode for sodium-ion batteries, J. Energy Storage, 64 (2023) 107242 https://doi.org/10.1016/j.est.2023.107242

[5] H.N. Vasavan, M. Badole, S. Saxena, V. Srihari, A.K. Das, P. Gami, S. Deswal, P. Kumar, S. Kumar, Impact of P3/P2 mixed phase on the structural and electrochemical performance of Na0.75Mn0.75Al0.25O2 cathode, J. Energy Storage, 74 (2023) 109428 https://doi.org/10.1016/j.est.2023.109428

[6] S. Saxena, M. Badole, H.N. Vasavan, V. Srihari, A.K. Das, P. Gami, S. Deswal, P. Kumar, S. Kumar, Deciphering the role of optimal P2/O3 phase fraction in enhanced cyclability and specific capacity of layered oxide cathodes, Chem. Eng. J., 485 (2024) 149921 https://doi.org/10.1016/j.cej.2024.149921

[7] T. Schmaltz, F. Hartmann, T. Wicke, L. Weymann, C. Neef, J. Janek, A Roadmap for Solid-State Batteries, Adv. Energy Mater., 13 (2023) 2301886 https://doi.org/10.1002/aenm.202301886

[8] Y. Lin, T. Wang, L. Zhang, X. Peng, B. Huang, M. Wu, T. Zhao, In-situ forming lithiophilic-lithiophobic gradient interphases for dendrite-free all-solid-state Li metal batteries, Nano Energy, 99 (2022) 107395 https://doi.org/10.1016/j.nanoen.2022.107395

[9] Z. Yao, J. Zhang, D. Yang, D. Zhang, B. Yang, F. Liang, Achieving Dendrite-Free Solid-State Lithium-Metal Batteries via In Situ Construction of Li3P/LiCl Interfacial Layers, ACS Appl. Mater. Interfaces, 16 (2024) 869 https://doi.org/10.1021/acsami.3c16118

[10] P. Albertus, V. Anandan, C. Ban, N. Balsara, I. Belharouak, J. Buettner-Garrett, Z. Chen, C. Daniel, M. Doeff, N.J. Dudney, B. Dunn, S.J. Harris, S. Herle, E. Herbert, S. Kalnaus, J.A. Libera, D. Lu, S. Martin, B.D. McCloskey, M.T. McDowell, Y.S. Meng, J. Nanda, J. Sakamoto, E.C. Self, S. Tepavcevic, E. Wachsman, C. Wang, A.S. Westover, J. Xiao, T. Yersak, Challenges for and Pathways toward Li-Metal-Based All-Solid-State Batteries, ACS Energy Lett., 6 (2021) 1399 https://doi.org/10.1021/acsenergylett.1c00445

[11] S. Xia, X. Wu, Z. Zhang, Y. Cui, W. Liu, Practical Challenges and Future Perspectives of All-Solid-State Lithium-Metal Batteries, Chem, 5 (2019) 753 https://doi.org/10.1016/j.chempr.2018.11.013

[12] S.A. Ahmed, T. Pareek, S. Dwivedi, M. Badole, S. Kumar, $LiSn_2(PO_4)_3$-based polymer-in-ceramic composite electrolyte with high ionic conductivity for all-solid-state lithium batteries, J. Solid State Electrochem., 24 (2020) 2407 https://doi.org/10.1007/s10008-020-04783-z

[13] T. Pareek, B. Singh, S. Dwivedi, A.K. Yadav, Anita, S. Sen, P. Kumar, S. Kumar, Ionic conduction and vibrational characteristics of Al^{3+} modified monoclinic $LiZr_2(PO_4)_3$, Electrochim. Acta, 263 (2018) 533 https://doi.org/10.1016/j.electacta.2018.01.087

[14] T. Pareek, S. Dwivedi, B. Singh, D. Kumar, P. Kumar, S. Kumar, $LiSnZr(PO_4)_3$: NASICON-type solid electrolyte with excellent room temperature Li^+ conductivity, J. Alloys Compd., 777 (2019) 602 https://doi.org/10.1016/j.jallcom.2018.10.384

[15] Z. Song, F. Chen, M. Martinez-Ibañez, W. Feng, M. Forsyth, Z. Zhou, M. Armand, H. Zhang, A reflection on polymer electrolytes for solid-state lithium metal batteries, Nat. Commun., 14 (2023) 4884 https://doi.org/10.1038/s41467-023-40609-y

[16] Z. Geng, Y. Huang, G. Sun, R. Chen, W. Cao, J. Zheng, H. Li, In-situ polymerized solid-state electrolytes with stable cycling for $Li/LiCoO_2$ batteries, Nano Energy, 91 (2022) 106679 https://doi.org/10.1016/j.nanoen.2021.106679

[17] B.W. Taklu, Y. Nikodimos, H.K. Bezabh, K. Lakshmanan, T.M. Hagos, T.A. Nigatu, S.K. Merso, H.Y. Sung, S.C. Yang, S.H. Wu, W.N. Su, B.J. Hwang, Air-stable iodized-oxychloride argyrodite sulfide and anionic swap on the practical potential window for all-solid-state lithium-metal batteries, Nano Energy, 112 (2023) 108471 https://doi.org/10.1016/j.nanoen.2023.108471

[18] H. Su, Y. Liu, Y. Zhong, J. Li, X. Wang, X. Xia, C. Gu, J. Tu, Stabilizing the interphase between Li and Argyrodite electrolyte through synergistic phosphating process for all-solid-state lithium batteries, Nano Energy, 96 (2022) 107104 https://doi.org/10.1016/j.nanoen.2022.107104

[19] D.A. Buchberger, P. Garbacz, K. Słupczyński, A. Brzezicki, M. Boczar, A. Czerwiński, Lithium Transport Studies on Chloride-Doped Argyrodites as Electrolytes for Solid-State Batteries, ACS Appl. Mater. Interfaces, 15 (2023) 53417 https://doi.org/10.1021/acsami.3c10857

[20] Z. Chen, H.P. Liang, Z. Lyu, N. Paul, G. Ceccio, R. Gilles, M. Zarrabeitia, A. Innocenti, M. Jasarevic, G.T. Kim, S. Passerini, D. Bresser, Ultrathin single-ion conducting polymer enabling a stable $Li|Li_{1.3}Al_{0.3}Ti_{1.7}(PO_4)_3$ interface, Chem. Eng. J., 467 (2023) 143530 https://doi.org/10.1016/j.cej.2023.143530

[21] X. Han, L. Gu, Z. Sun, M. Chen, Y. Zhang, L. Luo, M. Xu, S. Chen, H. Liu, J. Wan, Y.B. He, J. Chen, Q. Zhang, Manipulating charge-transfer kinetics and a flow-domain LiF-rich interphase to enable high-performance microsized silicon-silver-carbon composite anodes for solid-state batteries, Energy Environ. Sci., 16 (2023) 5395 https://doi.org/10.1039/d3ee01696j

[22] T. Li, P.K. Panda, C.-T. Hsieh, Y.A. Gandomi, P.-C. Yang, Lithium iron phosphate cathode supported solid lithium batteries with dual composite solid electrolytes enabling high energy density and stable cyclability, J. Energy Storage, 81 (2024) 110444 https://doi.org/10.1016/j.est.2024.110444

[23] F. Zhu, W. Deng, B. Zhang, H. Wang, L. Xu, H. Liu, Z. Luo, G. Zou, H. Hou, X. Ji, In-situ construction of multifunctional interlayer enabled dendrite-free garnet-based solid-state batteries, Nano Energy, 111 (2023) 108416 https://doi.org/10.1016/j.nanoen.2023.108416

[24] Y. Shi, Q. Li, X. Hu, Y. Liao, W. Li, Y. Xu, B. Zhao, J. Zhang, Y. Jiang, A tailored dual-layer electronic shielding interface enables highly stable and dendrite-free solid-state lithium metal batteries, Nano Energy, 120 (2024) 109150 https://doi.org/10.1016/j.nanoen.2023.109150

[25] A. Fu, J. Lin, J. Zheng, D.Y. Wu, Z. Zhang, P. Yan, Y. Su, C. Xu, J. Hao, H. Zheng, H. Duan, Y. Ding, J. Yan, S. Huang, C. Liu, C. Tang, X. Fang, Y. Yang, Additive evolved stabilized dual electrode-electrolyte interphases propelling the high-voltage Li||LiCoO2 batteries up to 4.7 V, Nano Energy, 119 (2024) 109095 https://doi.org/10.1016/j.nanoen.2023.109095

[26] M.J. Joo, M. Kim, S. Chae, M. Ko, Y.J. Park, Additive-Derived Surface Modification of Cathodes in All-Solid-State Batteries: The Effect of Lithium Difluorophosphate- and Lithium Difluoro(oxalato)borate-Derived Coating Layers, ACS Appl. Mater. Interfaces, 15 (2023) 59389 https://doi.org/10.1021/acsami.3c12858

[27] X. Zhou, Q. Ye, B. Pang, Z. Wu, T. Yang, W. Zhang, Y. Xia, H. Huang, X. Xia, X. He, Y. Gan, J. Zhang, Styrene-Butadiene-Styrene Block Copolymer-Li5.5PS4.5Cl1.5 Composite Solid-State Electrolyte Enabling a High-Performance All-Solid-State Lithium Battery, ACS Appl. Energy Mater., 6 (2023) 12120 https://doi.org/10.1021/acsaem.3c02579

[28] X. Yang, J. Liu, N. Pei, Z. Chen, R. Li, L. Fu, P. Zhang, J. Zhao, The Critical Role of Fillers in Composite Polymer Electrolytes for Lithium Battery, Nanomicro Lett., 15 (2023) 74 https://doi.org/10.1007/s40820-023-01051-3

[29] L. Yang, Q. Liu, H. Ma, Q. An, X. Wang, Y. Ding, Z. Mei, X. Sheng, L. Duan, J. Xie, H. Guo, Functional nanosheet fillers with fast Li+ conduction for advanced all-solid-state lithium battery, Energy Storage Mater., 62 (2023) 102954 https://doi.org/10.1016/j.ensm.2023.102954

[30] L. Wu, Y. Wang, M. Tang, Y. Liang, Z. Lin, P. Ding, Z. Zhang, B. Wang, S. Liu, L. Li, X. Guo, X. Yin, H. Yu, Lithium-ion transport enhancement with bridged ceramic-polymer interface, Energy Storage Mater., 58 (2023) 40 https://doi.org/10.1016/j.ensm.2023.02.038

[31] C. Tian, M. Song, J. Tang, H. Yuan, C. Ai, H. Cao, T. Huang, A. Yu, Rational Design of a Cross-Linked Composite Solid Electrolyte for Li-Metal Batteries, ACS Appl. Mater. Interfaces, 16 (2024) 1535 https://doi.org/10.1021/acsami.3c15456

[32] A.K. Das, M. Badole, H.N. Vasavan, S. Saxena, P. Gami, S. Kumar, Highly conductive ceramic-in-polymer composite electrolyte enabling superior electrochemical performance for all-solid-state lithium batteries, Ceram. Int., 49 (2023) 29719 10.1016/j.ceramint.2023.06.214

[33] T. Wang, Y. Mao, J. Wang, C. Sun, Dendrite-Free Lithium Metal Anodes Enabled by an Ordered Conductive Ni-Based Catecholate Interlayer for Solid-State Lithium Batteries, ACS Appl. Mater. Interfaces, 15 (2023) 53584 https://doi.org/10.1021/acsami.3c14152

[34] D.O. Shin, K. Oh, K.M. Kim, K.-Y. Park, B. Lee, Y.-G. Lee, K. Kang, Synergistic multi-doping effects on the $Li_7La_3Zr_2O_{12}$ solid electrolyte for fast lithium ion conduction, Scientific Reports, 5 (2015) 18053 https://doi.org/10.1038/srep18053

[35] X. Chen, T. Wang, W. Lu, T. Cao, M. Xue, B. Li, C. Zhang, Synthesis of Ta and Ca doped $Li_7La_3Zr_2O_{12}$ solid-state electrolyte via simple solution method and its application in suppressing shuttle effect of Li-S battery, J. Alloys Compd., 744 (2018) 386 https://doi.org/10.1016/j.jallcom.2018.02.134

[36] Y. Zhou, X. Li, Y. Yang, X. Huang, B. Tian, Production of Ta-Doped $Li_7La_3Zr_2O_{12}$ Solid Electrolyte with High Critical Current Density, ACS Appl. Energy Mater., 5 (2022) 13817 https://doi.org/10.1021/acsaem.2c02441

[37] Y. Li, Z. Wang, Y. Cao, F. Du, C. Chen, Z. Cui, X. Guo, W-Doped $Li_7La_3Zr_2O_{12}$ Ceramic Electrolytes for Solid State Li-ion Batteries, Electrochim. Acta, 180 (2015) 37 https://doi.org/10.1016/j.electacta.2015.08.046

[38] X. Zhang, T.-S. Oh, J.W. Fergus, Densification of Ta-Doped Garnet-Type $Li_{6.75}La_3Zr_{1.75}Ta_{0.25}O_{12}$ Solid Electrolyte Materials by Sintering in a Lithium-Rich Air Atmosphere, J. Electrochem. Soc., 166 (2019) A3753 https://doi.org/10.1149/2.1031915jes

[39] Z. Qin, Y. Xie, X. Meng, C. Shan, G. He, D. Qian, D. Mao, L. Wan, Y. Huang, High cycling stability enabled by Li vacancy regulation in Ta-doped garnet-type solid-state electrolyte, J. Eur. Ceram. Soc., 43 (2023) 2023 https://doi.org/10.1016/j.jeurceramsoc.2022.12.028

[40] H. El-Shinawi, E.J. Cussen, S.A. Corr, Enhancement of the lithium ion conductivity of Ta-doped $Li_7La_3Zr_2O_{12}$ by incorporation of calcium, Dalton Trans., 46 (2017) 9415 https://doi.org/10.1039/C7DT01573A

[41] V.K. Jayaraman, D.G. Porob, A.S. Prakash, Misconception in the Analysis of Tetragonal $Li_7La_3Zr_2O_{12}$ Garnet, ACS Appl. Energy Mater., 6 (2023) 11442 https://doi.org/10.1021/acsaem.3c01403

[42] X. Cheng, Q. Yan, R. Yan, X. Pu, Y. Jiang, Y. Huang, X. Zhu, Interfacial Modification of Ga-Substituted $Li_7La_3Zr_2O_{12}$ against Li Metal via a Simple Doping Method, ACS Appl. Mater. Interfaces, 15 (2023) 59534 https://doi.org/10.1021/acsami.3c14999

[43] R. Inada, A. Takeda, Y. Yamazaki, S. Miyake, Y. Sakurai, V. Thangadurai, Effect of Postannealing on the Properties of a Ta-Doped $Li_7La_3Zr_2O_{12}$Solid Electrolyte Degraded by Li Dendrite Penetration, ACS Appl. Energy Mater., 3 (2020) 12517 https://doi.org/10.1021/acsaem.0c02474

[44] A.J. Samson, K. Hofstetter, S. Bag, V. Thangadurai, A bird's-eye view of Li-stuffed garnet-type $Li_7La_3Zr_2O_{12}$ ceramic electrolytes for advanced all-solid-state Li batteries, Energy Environ. Sci., 12 (2019) 2957 https://doi.org/10.1039/c9ee01548e

[45] A. Coelho, TOPAS and TOPAS-Academic: an optimization program integrating computer algebra and crystallographic objects written in C++, J. Appl. Crystallogr., 51 (2018) 210 https://doi.org/10.1107/S1600576718000183

[46] T. Thompson, J. Wolfenstine, J.L. Allen, M. Johannes, A. Huq, I.N. David, J. Sakamoto, Tetragonal vs. cubic phase stability in Al-free Ta doped Li $_7La_3Zr_2O_{12}$ (LLZO), J. Mater. Chem. A, 2 (2014) 13431 https://doi.org/10.1039/c4ta02099e

[47] M.P. O'Callaghan, E.J. Cussen, Lithium dimer formation in the Li-conducting garnets $Li_{5+x}Ba_xLa_{3-x}Ta_2O_{12}$ $(0 < x \leq 1.6)$, Chem. Commun., 20 (2007) 2048 https://doi.org/10.1039/B700369B

[48] L.L. Wong, K.C. Phuah, R. Dai, H. Chen, W.S. Chew, S. Adams, Bond Valence Pathway Analyzer—An Automatic Rapid Screening Tool for Fast Ion Conductors within softBV, Chem. Mater., 33 (2021) 625 https://doi.org/10.1021/acs.chemmater.0c03893

[49] H. Chen, L.L. Wong, S. Adams, SoftBV - a software tool for screening the materials genome of inorganic fast ion conductors, Acta. Crystallogr. B., 75 (2019) 18 https://doi.org/10.1107/S2052520618015718

[50] K. Momma, F. Izumi, VESTA: a three-dimensional visualization system for electronic and structural analysis, J. Appl. Crystallogr., 41 (2008) 653 https://doi.org/10.1107/S0021889808012016

[51] W. Wieczorek, D. Raducha, A. Zalewska, J.R. Stevens, Effect of Salt Concentration on the Conductivity of PEO-Based Composite Polymeric Electrolytes, J. Phys. Chem. B, 102 (1998) 8725 https://doi.org/10.1021/jp982403f

[52] H. Zhuang, W. Ma, J. Xie, X. Liu, B. Li, Y. Jiang, S. Huang, Z. Chen, B. Zhao, Solvent-free synthesis of PEO/garnet composite electrolyte for high-safety all-solid-state lithium batteries, J. Alloys Compd., 860 (2021) 157915 https://doi.org/10.1016/j.jallcom.2020.157915

[53] D. Brouillette, D.E. Irish, N.J. Taylor, G. Perron, M. Odziemkowski, J.E. Desnoyers, Stable solvates in solution of lithium bis(trifluoromethylsulfone)imide in glymes and other aprotic solvents: Phase diagrams, crystallography and Raman spectroscopy, Phys. Chem. Chem. Phys., 4 (2002) 6063 https://doi.org/10.1039/b203776a

[54] Z. Wang, W. Gao, X. Huang, Y. Mo, L. Chen, Spectroscopic studies on interactions and microstructures in propylene carbonate - LiTFSI electrolytes, J. Raman Spectrosc., 32 (2001) 900 https://doi.org/10.1002/jrs.756

[55] Z. Li, H.-M. Huang, J.-K. Zhu, J.-F. Wu, H. Yang, L. Wei, X. Guo, Ionic Conduction in Composite Polymer Electrolytes: Case of PEO:Ga-LLZO Composites, ACS Appl. Mater. Interfaces, 11 (2019) 784 https://doi.org/10.1021/acsami.8b17279

[56] J. Evans, C.A. Vincent, P.G. Bruce, Electrochemical measurement of transference numbers in polymer electrolytes, Polymer, 28 (1987) 2324 https://doi.org/10.1016/0032-3861(87)90394-6

[57] X. He, Y. Yang, M.S. Cristian, J. Wang, X. Hou, B. Yan, J. Li, T. Zhang, E. Paillard, M. Swietoslawski, R. Kostecki, M. Winter, J. Li, Uniform lithium electrodeposition for stable lithium-metal batteries, Nano Energy, 67 (2020) 104172 https://doi.org/10.1016/j.nanoen.2019.104172

[58] C. Wang, J. Hong, Ionic/electronic conducting characteristics of $LiFePO_4$ cathode materials, Electrochem. Solid-State Lett., 10 (2007) A65 https://doi.org/10.1149/1.2409768

[59] L.X. Jiao, Z.Q. Li, Y.Z. Zhu, Z. Wei, Y. Liang, X.L. Wang, Y. Cui, Z.H. Zhang, M. He, B. Song, Enhanced electrical conductivity and lithium ion diffusion rate of $LiFePO_4$ by Fe site and P site doping, AIP Adv., 13 (2023) 2158 https://doi.org/10.1063/5.0159212

[Supplementary Material]

Integrated Cathode-Electrolyte ($Li_{6.55}La_3Zr_{1.55}Ta_{0.45}O_{12}$/PEO-LiTFSI)

[Supplementary Material]

Integrated Cathode-Electrolyte ($Li_{6.55}La_3Zr_{1.55}Ta_{0.45}O_{12}$/PEO-LiTFSI) Architecture Driven Excellent Performance of Solid-State Lithium Metal Batteries

Asish Kumar Das[a], Manish Badole[a], Hari Narayanan Vasavan[a], Samriddhi Saxena[a], Pratiksha Gami[a], Neha Dagar[a], Sunil Kumar [a,b,*]

[a]Department of Metallurgical Engineering and Materials Science, Indian Institute of Technology Indore, Simrol, 453552, India

[b]Center for Electric Vehicle and Intelligent Transport Systems, Indian Institute of Technology Indore, Simrol, 453552, India

*Corresponding author E-mail: sunil@iiti.ac.in

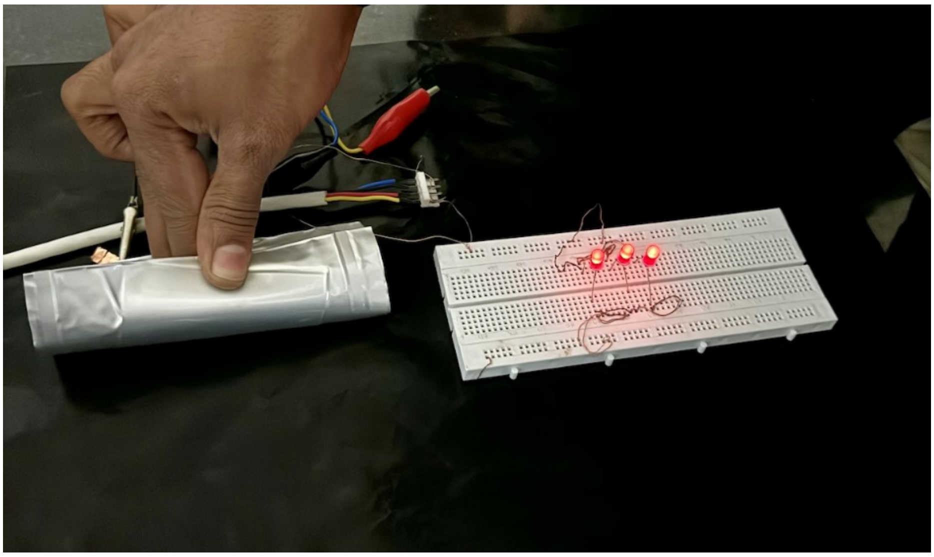

Figure S1. The flexibility nature of the fabricated solid-state pouch cell.

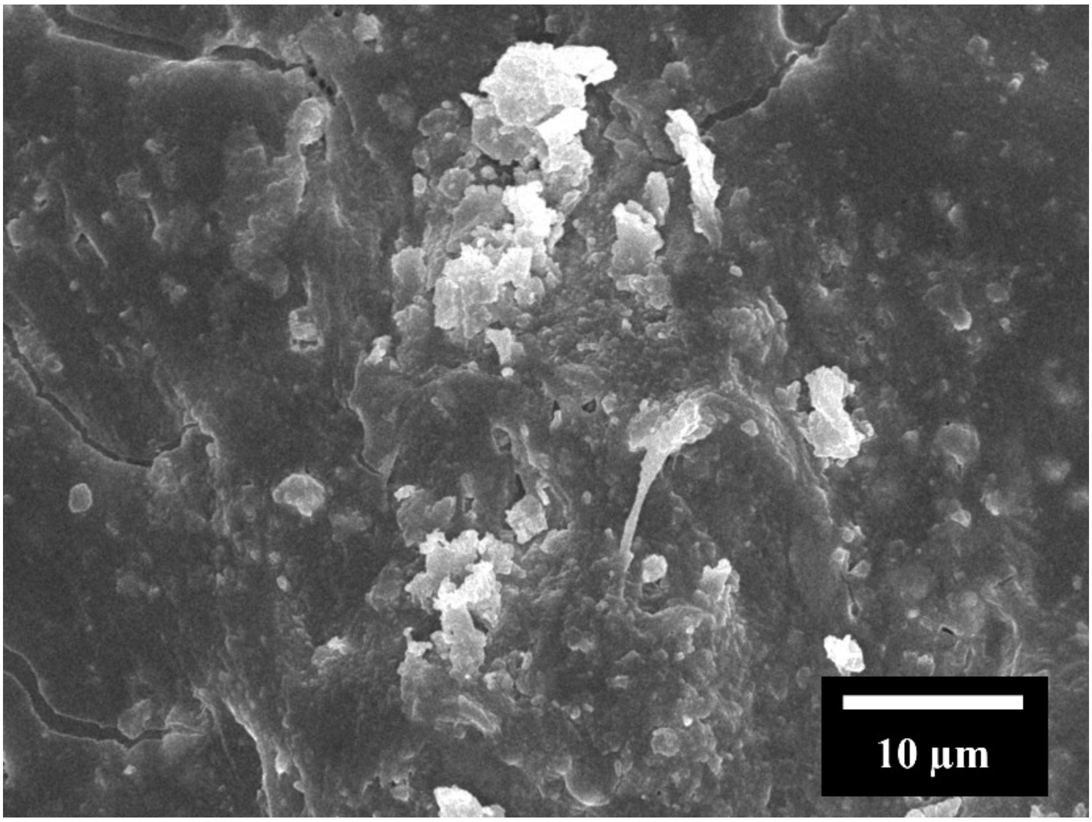

Figure S2. SEM image of SCE30 electrolyte.

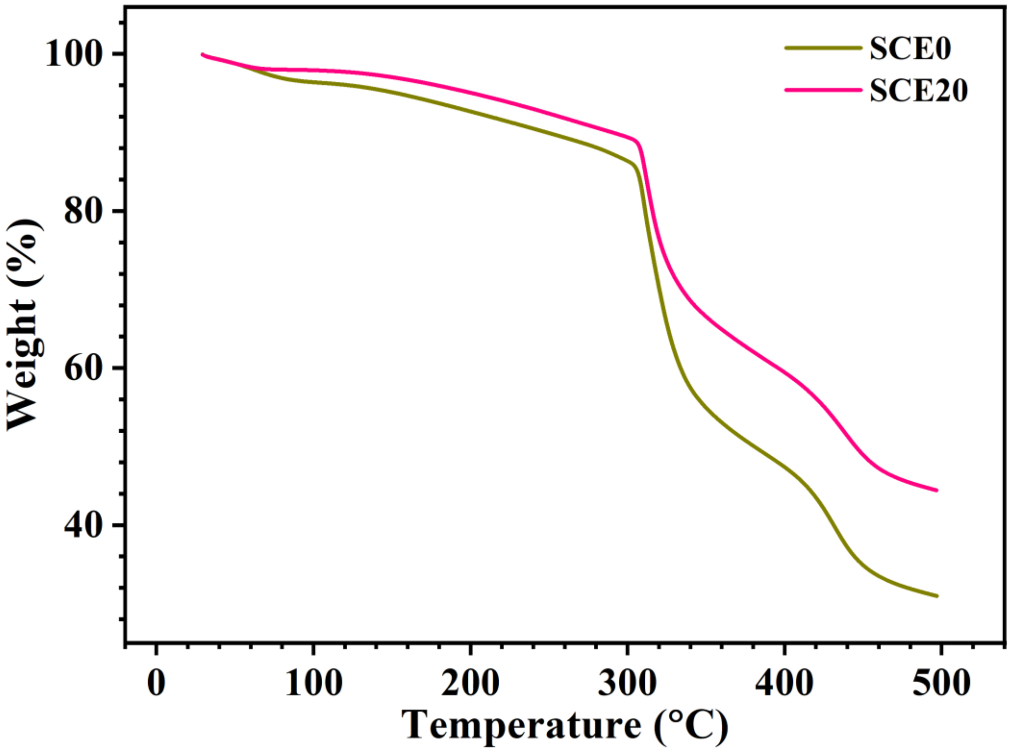

Figure S3. TGA data of SCE0 and SCE20 electrolyte samples.

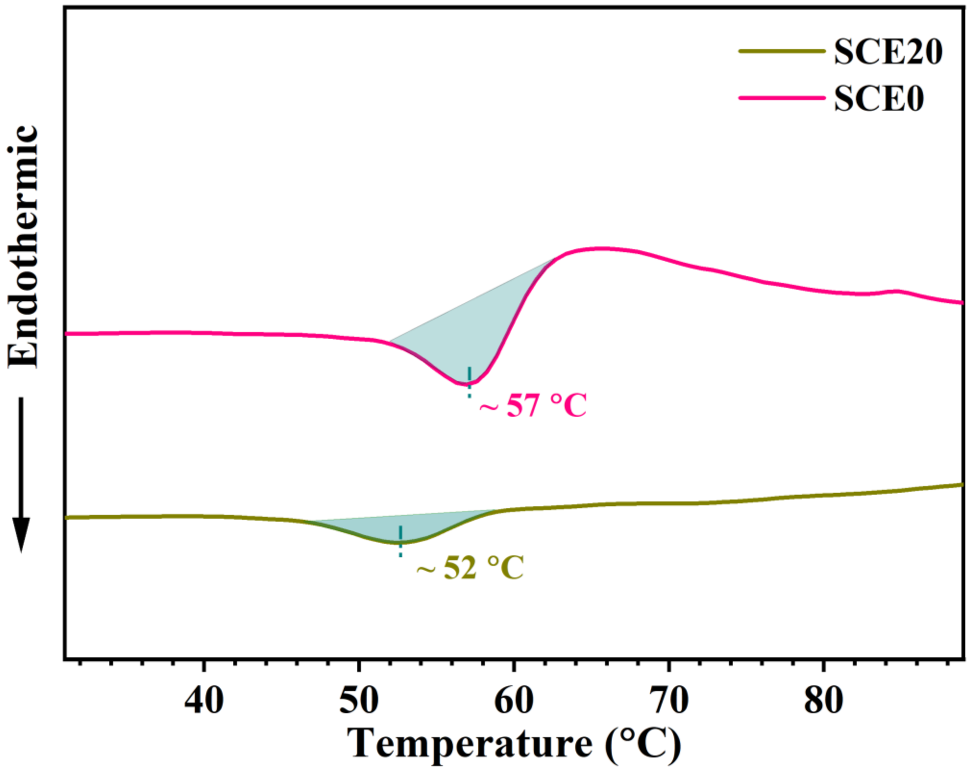

Figure S4. DSC data of SCE0 and SCE20 electrolyte samples.

Table S1. Comparison of studies Full-cell performance of Li||LiFePO$_4$ cells with composite electrolytes.

Composition	Initial discharge capacity	Number of cycles	Capacity retention	C-rate	Ref.
PVDF-HFP/PEG/LATP in-situ	126	1000	67.3	1C	[1]
BN/PEO	132	90	84	0.3C	[2]
PEO-butanedinitrile 3D PET	131	100	93.8	1C	[3]
LATP/PVDF-HFP	96.4	100	92.3	1C	[4]
PVDF-HFP/EDSN/BKT	145	450	86	0.3C	[5]
PEO/TiO2	156	550	54.2	0.5C	[6]
SPE-MEO-10	126.67	500	78.7	1C (60 °C)	[7]
PU/LLZTO	150	150	90	1C (60 °C)	[8]
PEG/LLZTO	157.5	150	89.7	0.1C (45 °C)	[9]
PEO/HPU-3	153.1	80	83.6	0.1C	[10]
PEO-LLZTO	~108	200	87.6	0.5C	[11]
PEO-LLZTO	**132**	**1000**	**84.2**	**1C (25 °C)**	**This work**

References:

[1] Q. Gai, T. Zhao, J. Ma, C. Wang, H. Gao, L. Li, An in-situ bicomponent polymeric matrix solid electrolyte for solid-state Lithium metal batteries with extended cycling-life, Journal of Energy Storage, 80 (2024) 110150. https://doi.org/10.1016/j.est.2023.110150

[2] X. Meng, D. Zhang, J. Mo, L. Liu, T. Yang, Q. Fan, Q. Zhao, R. Zhou, M. Zhang, W. Hou, W. Hu, W. Zhang, Y. Jin, B. Jiang, L. Chu, M. Li, Room-temperature solid-state metallic lithium batteries based on high-content boron nitride nanosheet-modified polymer electrolytes, Appl. Surf. Sci., 648 (2024). https://doi.org/10.1016/j.apsusc.2023.158962

[3] S. Yuan, Y. Luo, K. Xia, A. Zheng, G. Jiang, M. Fan, J. Xiong, C. Yuan, Z. Li, X. Wang, Developing flexible and safety-reinforced 3D polymer electrolytes based on polyethylene oxide for solid-state lithium metal batteries, Journal of Energy Storage, 78 (2024). https://doi.org/10.1016/j.est.2023.109853

[4] X. Wu, X. Jie, X. Liang, J. Wang, S. Wu, Ultraviolet-thermal coupling cross-linked fabricate polymer/ceramic composite solid electrolyte for room temperature quasi solid state lithium ion batteries, Journal of Energy Storage, 77 (2024). https://doi.org/10.1016/j.est.2023.109644

[5] V.A. Afrifah, J. Kim, I. Phiri, S.-Y. Ryou, Bikitaite composite polymer electrolyte for high-performance solid-state lithium metal battery, Journal of Industrial and Engineering Chemistry, 128 (2023) 412-419. https://doi.org/10.1016/j.jiec.2023.08.005

[6] Y. Su, Z. Mu, Y. Qiu, G. Jiang, A. Shenouda, X. Zhang, F. Xu, H. Wang, Embedding of Laser Generated TiO2 in Poly(ethylene oxide) with Boosted Li+ Conduction for Solid-State Lithium Metal Batteries, ACS Appl. Mater. Interfaces, 15 (2023) 55713-55722. https://doi.org/10.1021/acsami.3c12265

[7] T.G. Ritter, J.M. Gonçalves, S. Stoyanov, A. Ghorbani, T. Shokuhfar, R. Shahbazian-Yassar, AlTiMgLiO medium entropy oxide additive for PEO-based solid polymer electrolytes in lithium ion batteries, Journal of Energy Storage, 72 (2023) 108491. https://doi.org/10.1016/j.est.2023.108491

[8] Y. Gao, C. Wang, H. Wang, C. Feng, H. Pan, Z. Zhang, J. He, Q. Wang, Polyurethane/LLZTO solid electrolyte with excellent mechanical strength and electrochemical property for advanced lithium metal battery, Chem. Eng. J., 474 (2023). https://doi.org/10.1016/j.cej.2023.145446

[9] Y.-W. Song, S.-J. Park, K. Heo, H. Lee, D. Hwang, M.-Y. Kim, J. Kim, J. Lim, Enhancing Electrochemical Performance in PEO/LLZTO Composite Solid Electrolyte via PEG Polymer Integration for Solid-State Batteries, Energy Technol., 11 (2023) 2300334. https://doi.org/10.1002/ente.202300334

[10] W. Li, X. Zhu, N. Zhou, Y. Yang, R. Li, C. Wang, Z. Fang, X. Ma, W. Zhao, X. Fu, W. Yan, Helical Polyurethane-Initiated Unique Microphase Separation Architecture for Highly Efficient Lithium Transfer and Battery Performance of a Poly(ethylene oxide)-Based All-Solid-State Electrolyte, ACS Appl. Energy Mater., 4 (2021) 4772-4785. https://doi.org/10.1021/acsaem.1c00358

[11] T. Li, P.K. Panda, C.-T. Hsieh, Y.A. Gandomi, P.-C. Yang, Lithium iron phosphate cathode supported solid lithium batteries with dual composite solid electrolytes enabling high energy density and stable cyclability, Journal of Energy Storage, 81 (2024) 110444. https://doi.org/10.1016/j.est.2024.110444